Supporting Information

Unraveling the growth mechanism of $W_{18}O_{49}$ nanowires on W surfaces

Suresh Bandi, Ajeet K. Srivastav*

Department of Metallurgical & Materials Engineering, Visvesvaraya National Institute of Technology, Nagpur-440010.

Corresponding author: srivastav.ajeet.kumar@gmail.com

S.1: Experimental setup

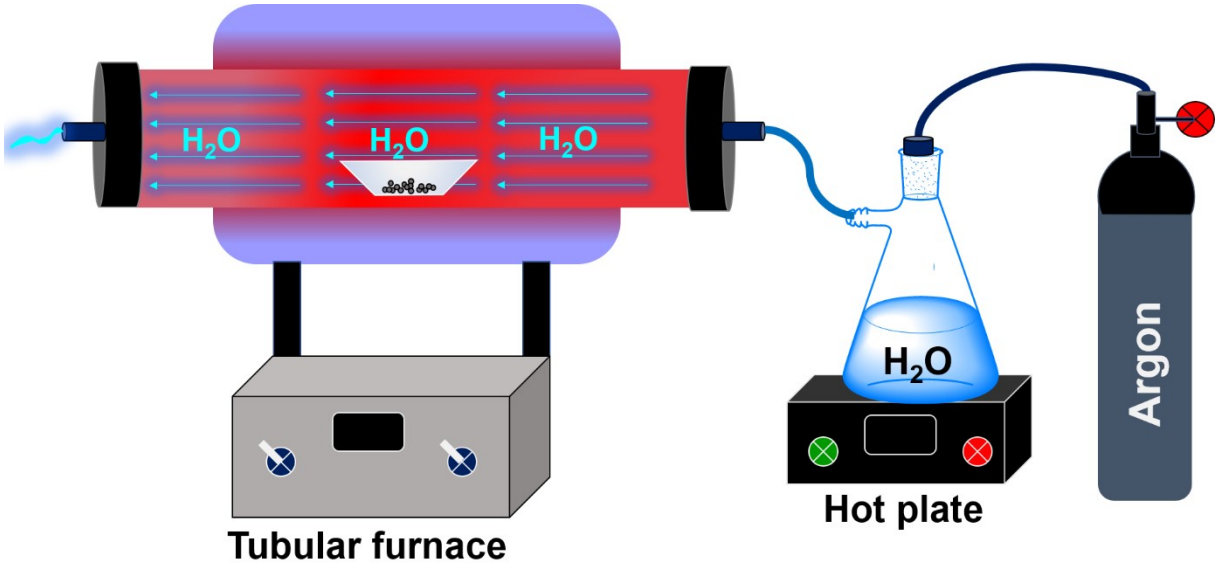

Figure S1. The schematic representation of the experimental setup for the heat treatment performed in the current work.

S.2: Characterization of precursor W

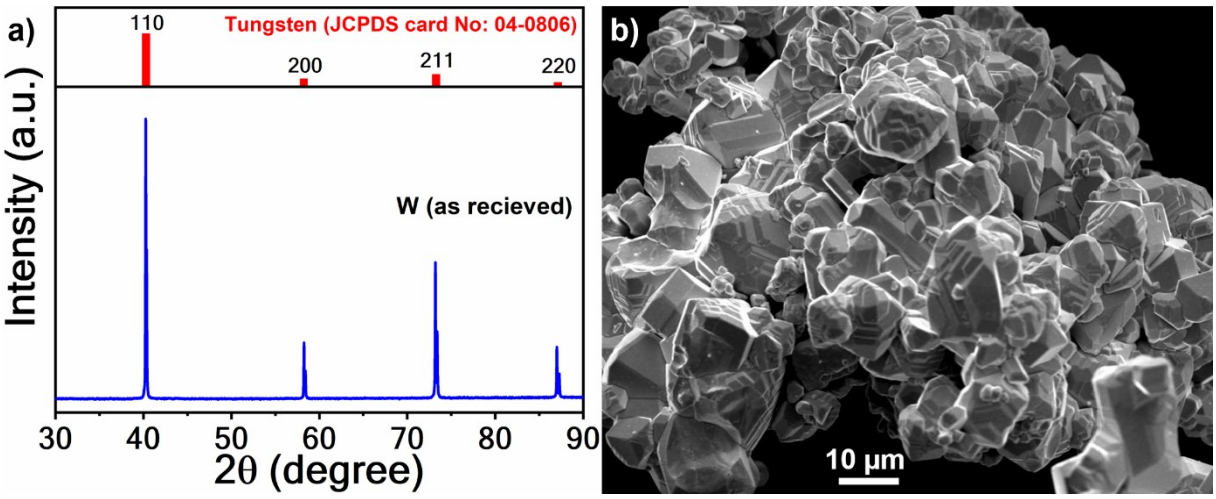

Figure S2. a) XRD profile of the precursor W powder and b) its SEM micrograph revealing irregular particle nature.

S.3: Appearance of the W powder obtained after thermal treatments

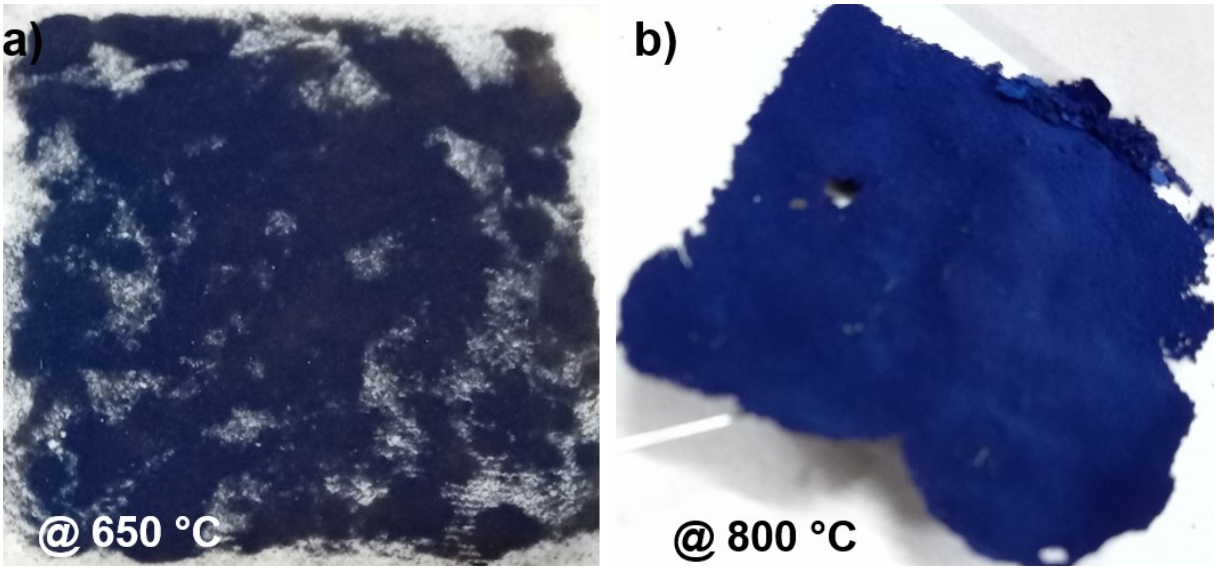

Figure S3. The appearance of final products after thermal treatments. a) W heat-treated at 650 °C/1h in $H_2O(v)$ atmosphere showing the bluish brown color. b) the sample heat-treated at 800 °C/1h showing lucent blue color.

S.4: Results of the intermediate thermal treatment at 450°C/1h

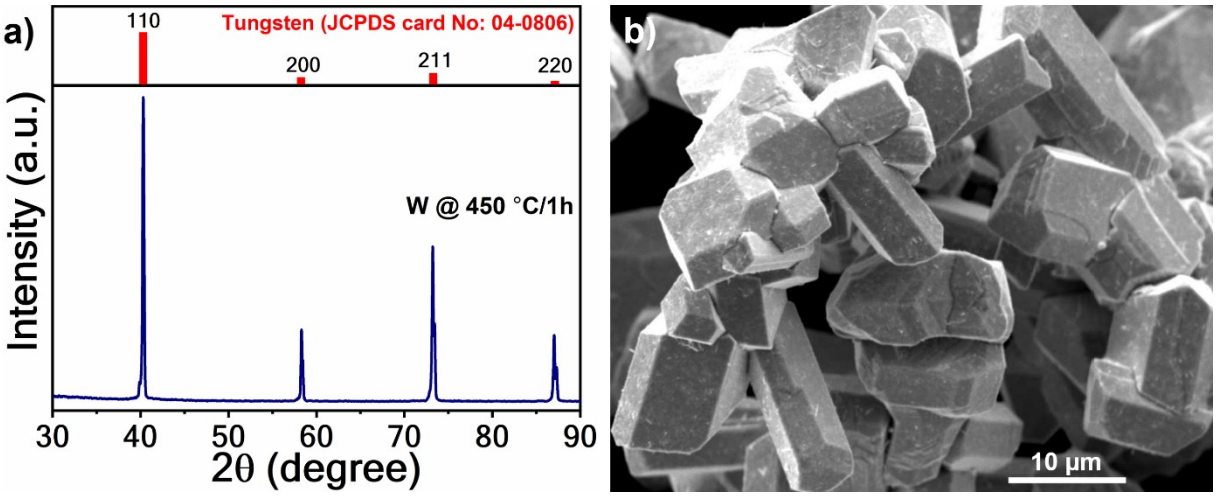

Figure S4. a) XRD and b) SEM micrographs of the W thermally treated at 450°C/1h under Ar+H_2O(v) atmosphere.

S.5: Dimensions of $W_{18}O_{49}$ NWs

The diameters and the lengths of the NWs are measured from the FESEM micrographs using ImageJ software (Ver 1.8.0_172). The statistics of the diameters obtained were varied from ~30 nm to ~400 nm. However, the NWs with a diameter <50 nm were not well resolved in the microscopy. The microscopic data is mostly dominated by the NWs with >150 nm. The average diameter of the NWs from the obtained data is calculated as 140±90 nm, as shown in **Figure S5**. Whereas the average length of the well resolved NWs was measured to be 6.5±1.5 µm. These statistics are compared with the other results from the literature where the thermal annealing routs were used for the synthesis.

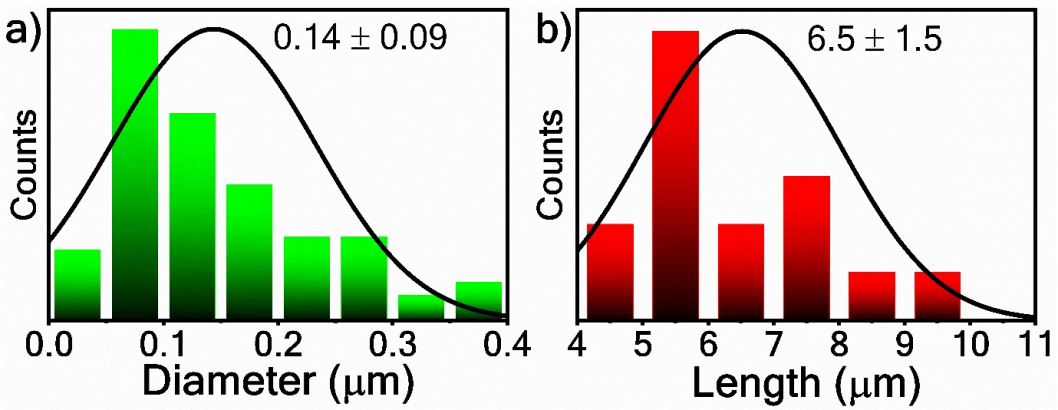

Figure S5. The size distributions of a) diameter and b) lengths of $W_{18}O_{49}$ NWs. The statistics were obtained from FESEM micrographs.

An attempt has been made to compare the product obtained in the current work with the same material reported in the literature. In this view, the details of the $W_{18}O_{49}$ 1d nanostructures synthesized via thermal annealing routes are collected. A comparison table consisting of precursor, temperature, furnace conditions, i.e., atmosphere, time, resultant phase, morphology, growth, and their dimensions, is made as shown in **Table S.1**.

Table S1. The comparison table of $W_{18}O_{49}$ 1*d* nanostructures obtained via thermal annealing routes.

Precursor	**Temp °C**	**Atmosphere**	**Time**	**Resultant phase & morphology**	**Growth mechanism**	**Relative content**	**Dia**	**Length**	**Ref.**
W	800	$H_2O(v)$	1 h	$W_{18}O_{49}$ NWs	SS ($H_2O(v)$ reaction induced)	Very high	30-400nm 140 nm (avg)	6.5 µm	C.W.
W	650	$H_2O(v)$	1 h	$W_{18}O_{49}$ NWs		Less	-	-	C.W.
W tip	700	Ar (O_2 leakage)	10 min	$W_{18}O_{49}$ NWs	VS (expected)	Less	10-30 nm	300 nm	[1]
W plate	700	Ar (O_2 leakage)	1 & 3 h	$W_{18}O_{49}$ NWs	VS (expected)	Very less	-	500 nm & 1.6 µm	[1]
W powder (0.6 - 1 µm)	800	Ar+ $H_2O(v)$	20,40 &120 min	$W_{18}O_{49}$ NNs	H_2O(v) reaction induced	Very high	20-400 nm	10-20 µm	[2]
100 mesh W powder	800		40 min	$W_{18}O_{49}$ NNs/NRs		Moderate	0.5-1 µm	10-20 µm	[2]
100 mesh W powder	1000		1 h	$W_{18}O_{49}$ MBs		High	-	~ 1mm	[2]
W foil (0.5mm thick)	800		40 min	$W_{18}O_{49}$ NNs		High	-	-	[2]
W wire (0.25 mm dia)	800		40 min	$W_{18}O_{49}$ NN bushes		High	-		[2]
W powders	1400 & 1300	Vacuum ~7.7 Pa, and Ar	0.5 h	$W_{18}O_{49}$ NTs	VS (expected)	High	-	~35 µm	[3]
Array of tungsten filaments (0.2 mm diameter)	1150	0.6 Torrr & Ar (O_2 leakage also)	0.5 h	$W_{18}O_{49}$ NWs	VS	High	100 nm	500 µm	[4]
	1200		0.5 h	$W_{18}O_{49}$ NBs	VS	High	200 nm, (30 nm each)		[4]
W powder	650	20 Torr	2 h	$W_{18}O_{49}$ NWs	VS	Less	10-50 nm	0.5 – 1.5 µm	[5]
W powder (0.2 µm)	600	Ar + $H_2O(v)$	0.5 h	$W_{18}O_{49}$ NWs	$H_2O(v)$ reaction induced	Moderate	20-50 nm	Several µm	[6]
WO_3 powder	900 to 1000	5-7 mTorr, and ~0.13 sccm air	3 h	$W_{18}O_{49}$ NWs	VS	High	10-20 nm	Few µm	[7]
Sputtered tungsten film	800	0.04-0.05 Pa, and 1-1.5 sccm O_2	0	$W_{18}O_{49}$ NWs	Solid phase	Less	-	-	[8]
W filament		0.8 Torr, and 200 sccm Ar	0.5 h	$W_{18}O_{49}$ NWs	VS	High	Several nm	Several µm	[4,9]
WO_3 powder	950,	0.1 and 1 Torr,	No soaking	$W_{18}O_{49}$ NWs	Thermal	Less	90-1000 nm	> 1 µm	[10]

	1000 and 1050	and Ar			evaporation/VS				
Milled W	1400	Ar	-	$W_{18}O_{49}$ NWs	Thermal evaporation/VS	Less	30-50 nm	700 nm	[11]
Sputtered tungsten film (150 nm thick)	650	15 Pa, Ar, and O_2 (0.1 sccm)	1 h	$W_{18}O_{49}$ NWs	Thermal Oxidative	Moderate	10-20 nm	0.5 – 1 µm	[12]
Amorphous W film	650	PLD (40 & 50 Pa)	10 h	$W_{18}O_{49}$ NWs	Vacuum annealing	Less	20-40 nm	0.85-0.36 µm	[13]
WO_3 powder covered with W sheet	1000	100 m Torr,	1 h	$WO_{2.9}$ NRs	VS (expected)	Moderate	80-400 nm	2-3 µm	[14]
W powder	1100	10 Pa, Ar (100 sccm) + O_2 (1 sccm)	1-20 min	$W_{18}O_{49}$ NWs	VS	Moderate	-	-	[15]
W Coin	1400	Ar (10 sccm)	10 h	$W_{18}O_{49}$ MRs	Thermal oxidative	Moderate	0.1 to few µm	Few µm	[16]
WO_3 Powder	1100	Ar and Sulphur at upstream	1 h	$W_{18}O_{49}$ MRs	VS	High/Moderate	Few µm	Few µm	[17,18]
Sputtered W films	550	Ar	1 h	$W_{18}O_{49}$ NWs	Thermal oxidative	Moderate	10-40 nm	400 nm	[19]

C.W.- current work, NWs- nanowires, NRs- nanorods, NBs- nanobundles, NNs- nanoneedles, MRs- microrods, MBs- microbundles, SS- solid solid, VS- vapor solid

S.6: W-O-H phase diagram

The W-O-H phase diagram is adapted from the literature.[20,21] The original version of the diagram consists of only X and Y-axis drawn as 10^3 T^{-1}(K) Vs $\frac{p[H_2]}{p[H_2O]}$. To improve the understandability, the diagram is implemented or redrawn here as a new figure with more elaboration in **Figure S6**. For a better understanding, a top X-axis showing the temperature in °C is added. The values of the same were calculated from the 10^3 T^{-1}(K) value of the bottom X-axis. Similarly, a new right Y-axis with $\%H_2O$ values, which were calculated from the $\frac{p[H_2]}{p[H_2O]}$ values of left Y-axis. Additionally, the crystal structures of the phases were given in their corresponding regions for the crystallographic representation.

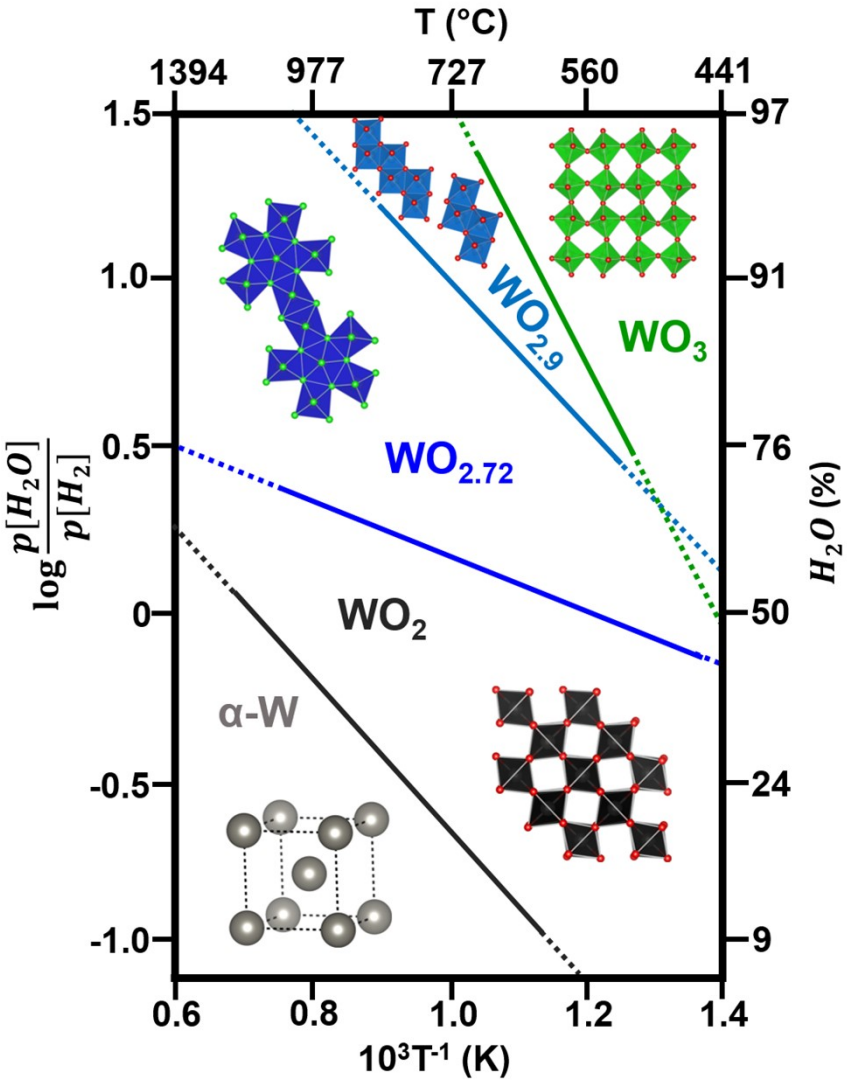

Figure S6. The equilibrium phase diagram showing the stability regions of tungsten oxides with respect to the $\%H_2O$ and temperature. The phase diagram is redrawn as reported elsewhere.[20,21]

S.7: XPS

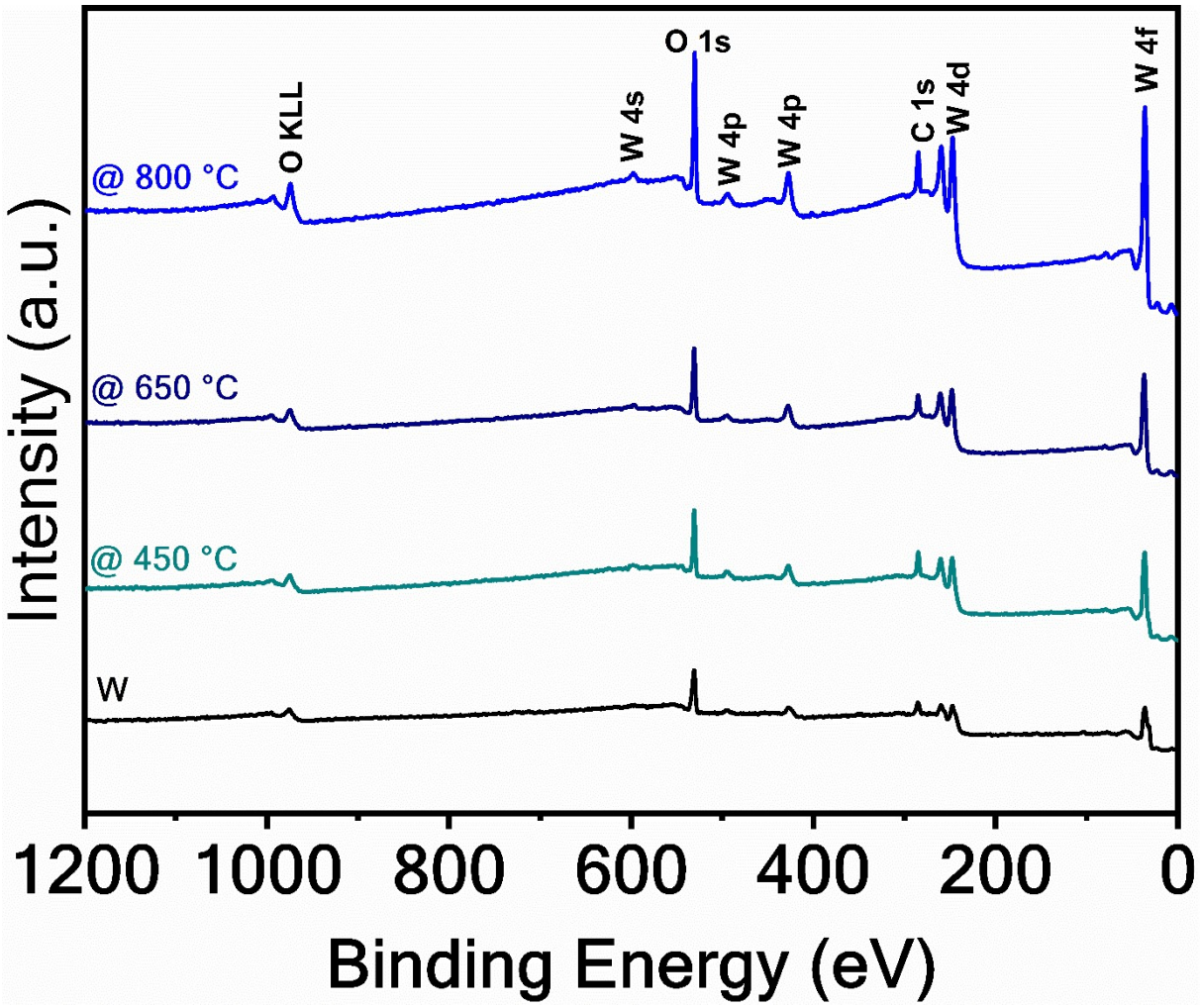

Figure S7. The XPS full survey of W, W@450°C, and W@650°C.

The binding energies corresponding to each peak obtained from the W 4f and O 1s spectra of all samples are tabulated in **Table S2**. Also, the percentages of the oxidation states were estimated using the area of peaks obtained after deconvolution.

Table S2. XPS peak positions of the W 4f spectra of W, W@450°C, W@650°C, and W@800°C.

W									
Peak	**$W5p_{3/2}$**	**$W^{6+}(W4f_{5/2})$**		**$W^{6+}(W4f_{7/2})$**	**W^{5+}**		**$W(W4f_{5/2})$**	**$W(W4f_{7/2})$**	
Position	41.63	37.73		35.63	-		33.4	31.28	
Area	2333.61	78900.06		103843.3	-		58096.8	60691.61	
%		**W^{6+} = 60.14**			**W^{5+} = 0**		**W = 39.09**		
W@450°C									
Position	41.459	39.31	37.828	35.77	36.763	34.32	33.601	32.235	31.47
Area	4318.76	1230.34	63760.04	71625.91	7575.27	28397.68	4284.37	2706.68	15192.95
%		**W^{6+} = 68.62**			**W^{5+} = 18.07**		**W = 11.14**		
W@650°C									
Position	41.146	38.073		36.119	37.652	34.953	-	31.646	
Area	13471.89	65992.42		73581.45	12993.46	59064.54	-	3013.02	
%		**W^{6+} = 61.18**			**W^{5+} = 31.59**		**W = 1.32**		
W@800°C									
Position	40.479	37.669	37.497	35.444	36.368	34.073	-	-	
Area	29440.28	78825.09	71701.22	129195.90	63464.28	104525.10	-	-	
%		**W^{6+} = 58.62**			**W^{5+} = 35.20**		**W = 0**		

References:

1 G. Gu, B. Zheng, W. Q. Han, S. Roth and J. Liu, 2002, **2**, 849–851.

2 Y. Z. Jin, Y. Q. Zhu, R. L. D. Whitby, N. Yao, R. Ma, P. C. P. Watts, H. W. Kroto and

D. R. M. Walton, *J. Phys. Chem. B*, 2004, **108**, 15572–15577.

3 J. Zhou, L. Gong, S. Z. Deng, J. Chen, J. C. She, N. S. Xu, R. Yang and Z. L. Wang, *Appl. Phys. Lett.*, 2005, **87**, 223108.

4 L. Chi, N. Xu, S. Deng, J. Chen and J. She, *Nanotechnology*, 2006, **17**, 5590–5595.

5 K. Hong, M. Xie and H. Wu, *Nanotechnology*, 2006, **17**, 4830–4833.

6 S. Shi, X. Xue, P. Feng, Y. Liu, H. Zhao and T. Wang, *J. Cryst. Growth*, 2008, **310**, 462–466.

7 K. Hong, M. Xie, R. Hu and H. Wu, *Appl. Phys. Lett.*, 2007, **90**, 173121.

8 Y. Kojima, K. Kasuya, K. Nagato, T. Hamaguchi and M. Nakao, *J. Vac. Sci. Technol. B Microelectron. Nanom. Struct.*, 2008, **26**, 1942–1947.

9 L. F. Chi, S. Z. Deng, N. S. Xu, J. Chen, J. C. She and X. H. Liang, *J. Phys. Conf. Ser.*, 2009, **188**, 012021.

10 N. Van Hieu, H. Van Vuong, N. Van Duy and N. D. Hoa, *Sensors Actuators B Chem.*, 2012, **171**–**172**, 760–768.

11 A. K. Srivastav, J. Basu, S. Kashyap, N. Chawake, D. Yadav and B. S. S. Murty, *Scr. Mater.*, 2016, **115**, 28–32.

12 Y. Qin, W. Xie, Y. Liu and Z. Ye, *Sensors Actuators B Chem.*, 2016, **223**, 487–495.

13 D. Dellasega, S. M. Pietralunga, A. Pezzoli, V. Russo, L. Nasi, C. Conti, M. J. Vahid, A. Tagliaferri and M. Passoni, *Nanotechnology*, 2015, **26**, 365601.

14 K. Senthil and K. Yong, *Nanotechnology*, 2007, **18**, 395604.

15 J. Y. Luo, F. Chen, Z. Cao, W. H. Zheng, H. C. Liu, Y. D. Li, G. T. Yang and Q. G. Zeng, *CrystEngComm*, 2015, **17**, 889–894.

16 L. Zhu, Z. Zhang, X. Ke, J. Wang, J. Perepezko and M. Sui, *Acta Mater.*, 2018, **148**, 55–62.

17 Z. Shen, Z. Peng, Z. Zhao and X. Fu, *Solid State Sci.*, 2018, **78**, 126–132.

18 W. Yu, Z. Shen, F. Peng, Y. Lu, M. Ge, X. Fu, Y. Sun, X. Chen and N. Dai, *RSC Adv.*, 2019, **9**, 7723–7728.

19 D. Spanu, S. Recchia, P. Schmuki and M. Altomare, *Phys. status solidi – Rapid Res. Lett.*, 2020, **14**, 2000235.

20 R. Haubner, W. Schubert, E. Lassner, M. Schreiner and B. Lux, *Int. J. Refract. Met. Hard Mater.*, 1983, **2**, 108–115.

21 E. Lassner and W.-D. Schubert, in *Tungsten properties, chemistry, technology of the element, alloys, and chemical compounds*, Kluwer Academic / Plenum Publishers, New York, 1998, pp. 85–132.